30th NENE 2021
September 6 - 9
BLED-SLOVENIA
International Conference Nuclear Energy for New Europe

Classification and Resolution Adaptive Drag Modelling of Gas-Liquid Interfaces with a Multifield Two-Fluid Model

Richard Meller, Benjamin Krull, and Fabian Schlegel
Institute of Fluid Dynamics, Helmholtz-Zentrum Dresden - Rossendorf
Bautzner Landstraße 400
01328 Dresden, Germany
r.meller@hzdr.de, b.krull@hzdr.de, f.schlegel@hzdr.de

Matej Tekavčič
Reactor Engineering Division, Jožef Stefan Institute
Jamova cesta 39
1000 Ljubljana, Slovenia
matej.tekavcic@ijs.si

ABSTRACT

Hybrid multiphase models recently become more established for numerically describing complex gas-liquid flows, combining two different numerical methods for distinct flow regimes. Both edge cases are proven to be capable of delivering reliable predictions. In order to improve the reliability for intermediate length scale ratios of grid size and interfacial structure, a procedure is proposed to classify interfaces by surrounding flow type and level of under-resolution. With this information the hydrodynamics in the interface region are controlled by means of a dedicated interfacial drag formulation in order to improve simulation results across several levels of spatial resolution. The functionality is demonstrated in a three-dimensional case of a gas bubble rising in stagnant liquid.

1 INTRODUCTION

Gas-liquid flows in industrial facilities generally show a broad range of length scales. For the predictions of those phenomena, hybrid multiphase models are being developed during the past years, e.g. [1, 2, 3, 4, 5]. The approach by Meller *et al.* [5] is described as hybrid multifield two-fluid model and will be the conceptual basis for the present work. The Euler-Euler model for small interfacial structures compared to the grid spacing is combined with a Volume-of-Fluid-like approach, capturing highly resolved interfacial structures. In both edge cases, i.e. very low and very high spatial resolution, the individual base models are proven to work as intended. For the Volume-of-Fluid-like mode of the present model the equivalence to the homogeneous model was demonstrated [5] and for the Euler-Euler mode, the model validation of Rzehak et al. [6] is named exemplary.

While the phase-specific velocity fields generally differ from each other (slip) in the regime of the Euler-Euler model, by definition no interfacial slip takes place in the fully resolved Volume-of-Fluid-like mode of the hybrid model, i.e. the individual phases stick together and move with the same velocity under all circumstances. In order to predict the dynamics of interfacial gas-liquid flows with intermediate spatial resolutions, the amount of interfacial slip

shall be controlled locally. Considering a rising gas bubble, which is poorly resolved, the lateral parts of the interface are associated with the interfacial shear layer and might undergo interfacial slip, i.e. locally phase-averaged gas and liquid velocities may differ considerably from each other. At the same time, at the top and bottom regions the gas velocity and the liquid velocity are very similar to each other, i.e. a no-slip condition is maintained between gas and liquid. To reflect these essential local differences, the present work focuses on the classification of the interface-surrounding flow. A measure is proposed for the degree of spatial under-resolution, which is similar to the well-known dimensionless wall-normal cell size in shear boundary layers of wall-bounded flows. This information is then used to control the amount of interfacial slip by means of a dedicated drag model for the interfacial momentum exchange. Functionality is demonstrated in a three-dimensional test case of a single gas bubble rising in stagnant liquid.

2 NUMERICAL METHOD

The hybrid multiphase model is based on the multifield two-fluid model [5]. The term *two-fluid* underlines the fact, that this work is based on the assumption of two (or more) interpenetrating continua. Individual physical phases might be described as a set of different numerical phases, which is expressed by the term *multifield*. For instance, gas is either be described as a continuous gas or as a dispersed gas, i.e. gas bubbles. The phase-averaged Navier-Stokes-Equations [7] consist of a continuity and a momentum balance equation for each individual phase α as shown in Eqs. 1 and 2, respectively.

$$\partial_t r_\alpha \rho_\alpha + \partial_i r_\alpha \rho_\alpha u_{\alpha,i} = 0 \tag{1}$$

$$\partial_t r_\alpha \rho_\alpha u_{\alpha,i} + \partial_j r_\alpha \rho_\alpha u_{\alpha,i} u_{\alpha,j} = -r_\alpha \partial_i p + \partial_j 2 r_\alpha \mu_\alpha S_{\alpha,ij} + r_\alpha g_i \rho_\alpha + \sum_{\beta \neq \alpha} r_\alpha \sigma_{\alpha\beta} \kappa_{\alpha\beta} n_{\alpha\beta,i} + f_{\alpha,i} \tag{2}$$

The phase-specific volume fraction, density, and viscosity are denoted as r_α, $\rho_\alpha = const$, and $\mu_\alpha = const$, respectively. The phase-averaged velocity vector is $\mathbf{u}_\alpha$, p is the pressure, shared between all phases, and $\mathbf{g}$ denotes the vector of gravity. The symbols $\sigma_{\alpha\beta}$, $\kappa_{\alpha\beta}$ and $\mathbf{n}_{\alpha\beta}$ denote the surface tension coefficient of the phase pair α and β, the curvature, and the normal vector of an interface, respectively. The phase-specific shear-rate tensor is $S_{\alpha,ij} = \frac{1}{2}\left(\partial_i u_{\alpha,j} + \partial_j u_{\alpha,i}\right) - \delta_{ij}\frac{1}{3}\partial_k u_{\alpha,k}$. The vector of interfacial momentum exchange is denoted $\mathbf{f}_\alpha$.

The equations are spatially discretised with a second order finite volume method and integrated in time with a semi-implicit Euler-scheme of first order accuracy. An interface compression term [8] is applied to the phase-fraction transport equations. Pressure-velocity coupling is realised via the *Compact Momentum Interpolation* Method [9]. The hybrid model is implemented in the *multiphaseEulerFoam* framework of the foundation release of the C++ library *OpenFOAM* [10]. The hybrid multiphase model is available under GPL license [11].

3 DETECTION OF UNDER-RESOLVED INTERFACE REGIONS

The basic idea is to assess the near interface shear flow in terms of the relative phase-specific velocity and of the interface orientation. The length scale of the computational grid cells is then related to a dimensionless shear-based length scale in the interface region, similarly to the dimensionless wall distance $y^+ = y/L_\tau$ in wall-bounded flows with wall-normal coordinate y and shear length scale L_τ [12]. In order to formulate such a measure, three different pieces of information are required: 1. the interface vector: $\mathbf{I}_{\alpha\beta} = r_\beta \nabla r_\alpha - r_\alpha \nabla r_\beta$, 2.

the phase-specific velocities of phase α: $\mathbf{u}_\alpha$ and 3. of phase β: $\mathbf{u}_\beta$. As typical for an algebraic Volume-of-Fluid(-like) method, i.e. one edge case of the utilised hybrid model, the interface is spread out across several grid cells. Hence, the three quantities named above are most meaningful in different locations across an interface region, i.e. locations where $0 < r_\alpha < 1$. That means, that the most reliable values are found in the centre of the interface region (1.) and at both sides of the interface, where either phase α (2.) or β (3.) are present. To make the required information available all across the finite interface region at a certain interface position, a transport of these quantities has to be realised. This is achieved via an iterative procedure, by which the information are transported step-wise across neighbouring grid cells along the negative gradient of each individual distribution of meaningfulness, i.e. $-\nabla|\mathbf{I}_{\alpha\beta}|$ (1.), $-\nabla r_\alpha$ (2.) and $-\nabla r_\beta$ (3.). In the course of this work, the procedure is repeated five times. The quantities resulting from this algorithm are denoted with superscript IF.

Finally, a meaningful value for each quantity of interest (1. to 3.) is available at each cell in the interface region. It is worth noting, that the procedure strictly avoids to gather velocity information from within the interface region because this is the region to be controlled. Instead, it clearly determines values related to positions very close to both sides of the interface. These are the proper values to control the interface region.

The relative flow field surrounding an interface region can be classified by its direction relative to the interface normal vector. One of two extreme cases is stagnation flow, in which the relative velocity between both fluids is directed perpendicular towards or away from the interface. The other extreme case is a shear flow, where both liquids have a relative flow velocity parallel to the interface. The degree of shear is expressed as the shear flow indicator according to Eq. 3.

$$\psi^{\mathrm{IF}} = \frac{|\mathbf{u}_\alpha^{\mathrm{IF}} - \mathbf{u}_\beta^{\mathrm{IF}} \times \mathbf{I}_{\alpha\beta}|}{|\mathbf{u}_\alpha^{\mathrm{IF}} - \mathbf{u}_\beta^{\mathrm{IF}}||\mathbf{I}_{\alpha\beta}|} \tag{3}$$

The indicator might take values between zero and one for flow types other than stagnation or shear, depending on the angle between relative velocity and interface normal. In order to estimate the degree of spatial under-resolution, the dimensionless interfacial cell size is defined, analogously to the theory of boundary layers in wall-bounded flows as shown in Eq. 4.

$$y^{+\mathrm{IF}} = \frac{\frac{1}{|\mathbf{I}_{\alpha\beta}^{\mathrm{IF}}|}}{L^*} \tag{4}$$

The inverse of $|\mathbf{I}_{\alpha\beta}^{\mathrm{IF}}|$ is a rough approximation for the interface thickness and is based on the assumption, that the phase volume fractions are distributed linearly across the interface. Analogous to the *viscous length scale* in wall bounded flows [12], the *shear length scale* L^* is calculated from the relative interfacial velocity $\mathbf{u}_\alpha^{\mathrm{IF}} - \mathbf{u}_\beta^{\mathrm{IF}}$ and the interface normal vector $\mathbf{I}_{\alpha\beta}^{\mathrm{IF}}$, which are obtained as described before. As for wall-bounded flows, it is assumed, that a dimensionless interfacial cell size $y^{+\mathrm{IF}} < 1$ indicates a complete resolution of the shear boundary layer, meaning, that all relevant velocity gradients are captured on the computational grid. The larger this quantity, the higher is the assumed degree of under-resolution. Based on both the shear flow indicator ψ^{IF} and dimensionless interfacial cell size $y^{+\mathrm{IF}}$, the under-resolution indicator is proposed in Eq. 5.

$$f^{\mathrm{UR}} = \begin{cases} \psi^{\mathrm{UR}} \left(1 - e^{1-y^{+\mathrm{IF}}}\right) & \text{, if } y^{+\mathrm{IF}} > 1 \\ 0 & \text{, otherwise} \end{cases} \tag{5}$$

This quantity becomes one in case of a fully under-resolved shear flow at the respective interface position. If the flow is either of stagnation type or considered fully resolved, the indicator takes the value zero. For other cases, f^{UR} might take values between zero and one.

4 ADAPTIVE DRAG MODELLING

Based on the proposed criterion for detecting under-resolved interface regions, an adaptive drag formulation is derived. In order to achieve tight coupling of phase-specific velocity fields for resolved interfaces (Volume-of-Fluid-like mode of the hybrid model), the interfacial drag formulation of Štrubelj and Tiselj [13] is adopted. From now on, this drag model is referred as *resolving* drag model, which is indicated by the superscript R for the drag coefficient $K^{\mathrm{D,R}}$. The relaxation time in this model formulation is set to 10^{-8} times the physical time step, which results in a negligible relative velocity between phases α and β. The two-fluid model collapses towards the homogeneous model in case of an infinite drag coefficient, which is shown analytically [14]. This functionality is demonstrated in the context of the currently used hybrid model approach [5].

Considering a fully under-resolved rising gas bubble, the integral drag formulation considering a drag coefficient C_d [15] has turned out to be a valid approach for the interfacial drag coupling [16]. This constant is proposed to be set to $C_d = 0.22$ in order to reproduce consistent bubble rising velocities [16]. With the hybrid model formulation under investigation, this turns out to predict disintegration of a gas bubble on coarse computational grids. A value of $C_d = 0.8$ has shown to be better suited for this kind of problem and, hence, is used hereafter. This drag model is called *under-resolving* drag model and the according drag coefficient is marked with the superscript UR for drag coefficient $K^{\mathrm{D,UR}}$.

As the values of both drag formulations named above span several magnitudes, a simple linear interpolation appears to be inappropriate. In analogy to the electrical conductivity, linear combination of inverse drag coefficients results in Eq. 6.

$$K^{\mathrm{D}} = \frac{K^{\mathrm{D,UR}} K^{\mathrm{D,R}}}{K^{\mathrm{D,UR}} + f^{\mathrm{UR}} K^{\mathrm{D,R}}} \tag{6}$$

This formulation effectively blends between the resolving drag formulation for $f^{\mathrm{UR}} = 0$ and the under-resolving one for $f^{\mathrm{UR}} = 1$. The formulation is referred as *resolution adaptive* drag model.

5 APPLICATION TO THREE-DIMENSIONAL RISING GAS BUBBLE

In order to assess the framework of interface classification and adaptive drag modelling as described before, a three-dimensional test case is selected, which is proposed by Adelsberger *et al.* [17]. It features a three-dimensional single gas bubble initialised as sphere with diameter D_b and rising in stagnant liquid under the influence of gravity. Gas and liquid are initially assumed to be at rest. The computational domain has a cuboid shape with dimensions of $2D_b \times 2D_b \times 4D_b$ in the three respective spatial directions. All boundaries are considered to be no-slip walls, i.e. phase-specific velocities are zero at the wall and the pressure gradient in wall normal direction is set to zero.

The selected test case is originally denoted with Case 2 [17] and is characterised by the following dimensionless numbers: ratios of density and dynamic viscosity between liquid and gas of 1000 and 100, respectively, an Eötvös number $Eo = 125$, and a Reynolds number based on the gravitational velocity $Re_g = 15$. The domain is spatially discretised with a regular

computational grid with cubical cells. The reference data [17], which was produced with the OpenFOAM solver *interFoam*, are obtained on a grid with $128 \times 256 \times 128$ grid cells. It turns out, that those results can be reproduced quite well with the resolving drag model and an identical grid resolution considering the bubble shape and rising velocity.

5.1 Resolving Drag Model

In order to assess the performance of the used hybrid model, four different computational G1 to G4 are used. Detailed information about the different grids are listed in Tab. 1, which includes the ratio of cell size Δ_x to sphere-equivalent bubble diameter D_b besides the number of grid cells in each direction. The results are presented in Fig. 1. The gas-liquid interface

Table 1: Overview over different computational grids for mesh study.

Computational Grid	G1	G2	G3	G4
Number of grid cells	$8 \times 16 \times 8$	$16 \times 32 \times 16$	$32 \times 64 \times 32$	$64 \times 128 \times 64$
Δ_x/D_b	4	8	16	32

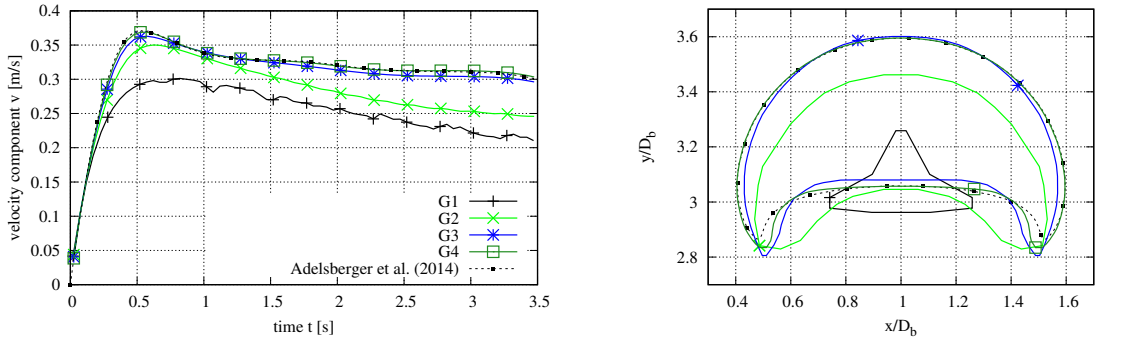

(a) Bubble rising velocity over time

(b) interface position ($\alpha_\mathrm{G} = 0.5$) at $t = 3.5$ s

Figure 1: Results of grid study obtained with resolving drag model $K^{\mathrm{D,R}}$.

position in the reference data are scaled and translated in order to match the current results. Hence, the reference data in Fig. 1 b) can purely serve for comparison of the shape of the bubble. As expected from the reference data, the bubble initially accelerates from rest and reaches a temporary maximum rising velocity before maintaining a nearly constant velocity with a slightly lower value. Finally the bubble starts to decelerate slightly for $t > 3$ s, as it approaches the upper wall. The bubble rising velocity predicted with grid G4 is nearly identical to the reference data, while a strong underestimation is observed on the coarse grids, especially with G1. The temporary velocity maximum is reached too late and the value is $5.7\,\%$ and $18.9\,\%$ lower with G2 and G1, respectively. Subsequently, the gas bubble continues decelerating further with these two grids instead of rising with nearly constant velocity.

Considering the bubble shape in Fig. 1 b), the result obtained with G4 is very close to the reference results, except for the tips of both ligaments at the bottom of the bubble being slightly less sharp. Grid G3 reveals a more narrow bubble shape with more elongated ligaments and the bubble reaches a slightly lower vertical position compared to G4. A lower vertical position is reached at $t = 3.5$ s on the coarse grids G1 and G2 compared to G4, which results directly from the reduced rising velocity as discussed before. On computational grid G2, the bubble is deformed in such a way, that its shape is narrower and more bend, resulting in a curved shape

of the interface at the centre bottom of the gas bubble. The bubble shape obtained with G1 differs even more from the reference data as it shows a peak at the top of the gas structure. The generally small size of the bubble is explained with the strong smearing of the interface due to the low spatial resolution.

Therefore, the resolving drag model is assessed to be a reasonable approach for high spatial resolution, which allows to reproduce simulation results of the homogeneous model. On coarse computational grids, this drag formulation delivers a bubble rising velocity, which is too slow, while the gas bubble is deformed in a nonphysical way.

5.2 Under-Resolving Drag Model

As pointed out in Sec. 4, the drag formulation with a constant coefficient of $C_d = 0.8$ is used for cases, in which an interfacial slip velocity is allowed across the volume of the whole gas bubble. Considering the same computational grids as in the previous section, a similar grid refinement study is carried out with the under-resolving drag formulation. The results are shown in Fig 2. The reference data in Fig. 2 b) has the same scaling and offset as in Fig. 1 b).

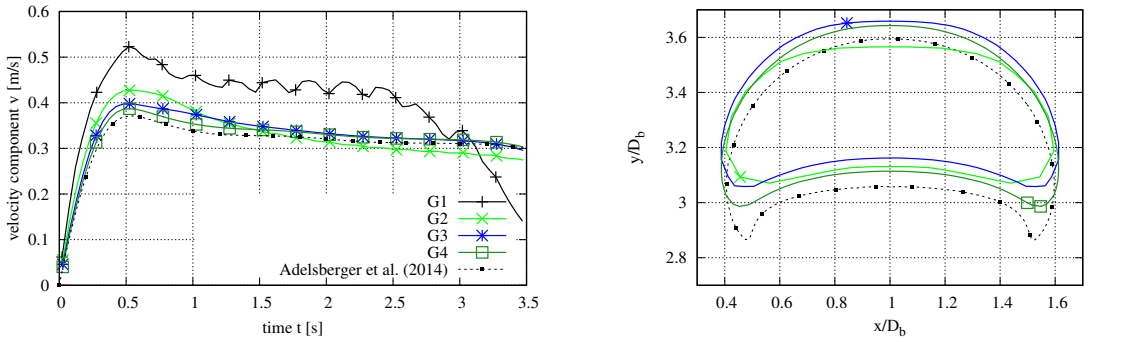

(a) Bubble rising velocity over time

(b) interface position ($\alpha_G = 0.5$) at $t = 3.5$ s

Figure 2: Results of grid study obtained with under-resolving drag formulation $K^{\mathrm{D,UR}}$.

Considering the bubble rising velocity in Fig. 2 a), it is evident, that the bubble is predicted to rise too fast on coarse grids, especially G1, compared to the reference data. With G1, the maximum vertical velocity is overestimated by 40.8 %. In the following period, the bubble rising velocity is oscillating and is higher than the reference value until $t = 3.1$ s. Subsequently, the velocity drops rapidly, because the gas bubble reaches the top boundary of the computational domain too early. With grid G2, the bubble decelerates too much after reaching its maximum velocity. In contrast to the resolving drag model, on the fine grid G4, the rising velocity is too high throughout the whole time. The velocity is overestimated by 4.2 % at its maximum and does not reach the reference value until $t = 3.5$ s.

Considering the interface position shown in Fig. 2 b), with grid G1, at $t = 3.5$ s the gas structure reached the top wall ($y = 2$ m), which is in line with the strong over-prediction of the rising velocity. Hence, the data is out of the shown range in this case. On all other computational grids under investigation, the bubble is too flat compared to the reference data and no sharp ligaments are observed at all. Hence, it is assumed, that with the under-resolving drag formulation the convergence rate of the results towards the reference values is extremely low, if the latter are even achieved at any level of spatial resolution.

5.3 Resolution Adaptive Drag Model

The interface classification approach presented in Sec. 3 and the resolution drag formulation described in Sec. 4 are assessed in combination with the same grid refinements study. The resulting under-resolution indicator f^{UR} is shown in Fig. 3. It is evident, that the most degree

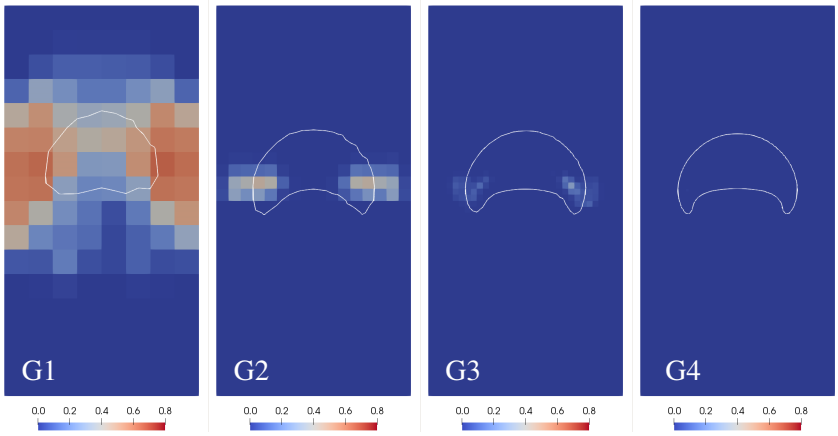

Figure 3: Under-resolution indicator f^{UR} as contour of the xy-plane and interface position ($\alpha_{\mathrm{G}} = 0.3$) marked as white line for all four computational grids for three-dimensional rising gas bubble.

of under-resolution is detected on G1 at the lateral positions of the gas bubble with a maximum value of $f^{\mathrm{UR}}_{max} \approx 0.7$. In this region the highest shear rate is expected, which demonstrates the functionality of the classification procedure. Consequently lower values of f^{UR} are calculated at the stagnation points on the top and the centre bottom points of the bubble surface. With increasing spatial resolution, the region of detected under-resolution and the maximum predicted value of f^{UR} become smaller. On G4 full resolution is predicted with $f^{\mathrm{UR}} = 0$.

The grid study results are presented in Fig. 4. The reference data in Fig. 4 b) has the same scaling and offset as in Fig. 1 b). While the rising velocity in Fig. 4 a) predicted with G1

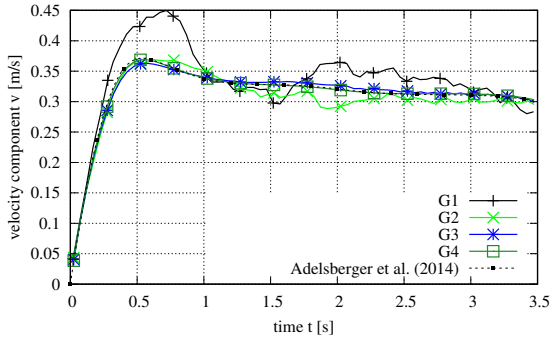

(a) Bubble rising velocity over time

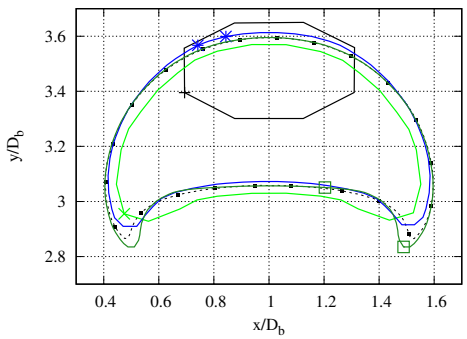

(b) interface position ($\alpha_{\mathrm{G}} = 0.5$) at $t = 3.5$ s

Figure 4: Results of grid study obtained with resolution adaptive drag formulation K^{D}.

still overshoots the reference data until reaching its temporary maximum, the deviation is much smaller compared to the under-resolving drag formulation with a overestimation of 21.1 %. Hence, the error is approximately half as large as with the under-resolving drag model. After reaching the highest rising velocity, with G1 the bubble decelerates and the deviation from the reference data shrinks. With grid G2, a rising velocity is predicted, which is much closer to the

reference data than with both the resolving and the under-resolving drag formulations with the same spatial resolution. The results with G4 are quasi identical to the resolving drag formulation on G4 and, hence, almost no error is observed when compared to the reference data.

Considering the bubble shape in Fig. 4 b), the solution obtained with G1 reveals, that the gas bubble is located slightly ahead of the position obtained with G4, but the difference is minor compared to result G1 with the under-resolving drag formulation. The bubble shape obtained with this grid is flat and shows no ligaments. It is worth noting, that grid G1 corresponds to a spatial resolution of four grid cells per sphere-equivalent bubble diameter, thus it is mathematically impossible to capture more complex shapes on such a grid. For grids G2 to G4, convergent bubble shapes are observed resulting in minor deviations from the reference solution with G4.

In this test case, the resolution adaptive drag modelling framework delivers results, which are reasonable across all levels of grid refinement under investigation improving especially the solution on very coarse computational grids. In contrast, the under-resolving drag formulation with a fixed drag coefficient all across the computational domain turns out to deliver unreliable results for all levels of spatial resolution. For fine grids, the solution of the adaptive drag model converges towards the Volume-Of-Fluid-like solution obtained with the resolving drag formulation and, hence, is quite close to the reference data.

6 CONCLUSION AND PERSPECTIVE

Based on the hybrid multifield two-fluid model [5], a procedure is proposed, which allows a proper modelling of gas-liquid interfaces even on very coarse meshes. For this purpose, two characteristics are determined locally: the type of flow surrounding the interface and the degree of spatial resolution of the interfacial shear layer. The resulting indicator function detects regions of under-resolution, which can be used to adapt the drag locally, allowing local interfacial slip. This is realised as a blending between resolving and under-resolving drag. The functionality of this framework is demonstrated in the case of a 3D gas bubble rising in stagnant liquid. It is shown, that the solution converges towards the reference data for high spatial resolutions, just as expected. However, it is remarkable that the present approach predicts bubble rising velocity and shape reasonably well for all lower grid resolutions. This contributes to a hybrid model, which will help to predict gas-liquid flow by means of arbitrary degree of spatial resolution with reliable predictive power.

Application of this framework to stratified flows as well as to more complex and industrially relevant test cases might be focus of future endeavours. Furthermore, the information about the estimated degree of under-resolution might be used for other modelling aspects in the context of multiphase flow simulation, such as turbulence damping in the vicinity of the interface or controlled morphology transitions between continuous and disperse phases and vice-versa.

ACKNOWLEDGMENTS

This work was supported by the Helmholtz European Partnering Program in the project *Crossing borders and scales (Crossing)*. The authors gratefully acknowledge the financial support provided by the Slovenian Research Agency through the grant P2-0026.

REFERENCES

[1] A. De Santis, M. Colombo, B. C. Hanson, M. Fairweather, “A generalized multiphase modelling approach for multiscale flows”, J. Comput. Phys., 436, 2021, p. 110321.

[2] A. Mathur, D. Dovizio, E. M. A. Frederix, E. M. J. Komen, “A Hybrid Dispersed-Large Interface Solver for multi-scale two-phase flow modelling”, Nucl. Eng. Des., 344, 2019, pp. 69–82.

[3] P. Coste, J. Laviéville, J. Pouvreau, C. Baudry, M. Guingo, A. Douce, “Validation of the Large Interface Method of NEPTUNE CFD 1.0.8 for Pressurized Thermal Shock (PTS) applications”, Nucl. Eng. Des., 253, 2012, pp. 296–310.

[4] E. K. Wardle, H. G. Weller, “Hybrid Multiphase CFD Solver for Coupled Dispersed/Segregated Flows in Liquid-Liquid Extraction”, Int. J. Chem. Eng., 2013, p. 128936.

[5] R. Meller, F. Schlegel, D. Lucas, “Basic verification of a numerical framework applied to a morphology adaptive multifield two-fluid model considering bubble motions”, Int. J. Numer. Meth. Fluids, 93(3), 2021, pp. 748–773.

[6] R. Rzehak, T. Ziegenhein, S. Kriebitzsch, E. Krepper, D. Lucas, “Unified Modeling of Bubbly Flows in Pipes, Bubble Columns, and airlift columns”, Chem. Eng. Sci., 157, 2017, pp. 147–158.

[7] D. A. Drew, S. L. Passman, “Theory of multicomponent fluids”, 135, Springer Science & Business Media, New York, 2006, pp. 310.

[8] H. G. Weller, “A new approach to VOF-based interface capturing methods for incompressible and compressible flow”, OpenCFD Ltd., Report TR/HGW, 4, 2008.

[9] A. Cubero, A. Sánchez-Insa, N. Fueyo, “A consistent momentum interpolation method for steady and unsteady multiphase flows”, Comput. Chem. Eng., 62, 2014, pp. 96–107.

[10] The OpenFOAM Foundation Ltd., “OpenFOAM-dev”, https://openfoam.org/, https://github.com/OpenFOAM/OpenFOAM-dev/, commit 28745ec, June 12th 2021.

[11] F. Schlegel, M. Draw, I. Evdokimov, S. Hänsch, H. Khan, R. Lehnigk, R. Meller, G. Petelin, M. Tekavčič, “HZDR Multiphase Addon for OpenFOAM”, Version 2.1.0, 2021.

[12] S. B. Pope, “Turbulent flows”, Cambridge University Press, Cambridge, 2000, pp. 771.

[13] L. Štrubelj, I. Tiselj, “Two-fluid model with interface sharpening”, Int. J. Numer. Meth. Eng., 85(5), 2011, pp. 575–590.

[14] K. Yan, D. Che, “A coupled model for simulation of the gas-liquid two-phase flow with complex flow patterns”, Int. J. Multiph. Flow, 36(4), 2010, pp. 333–348.

[15] M. Ishii, K. Mishima, “Two-fluid model and hydrodynamic constitutive relations’, Nucl. Eng. Des., 82(2-3), 1984, pp. 107–126.

[16] F. Gauss, D. Lucas, E. Krepper, “Grid studies for the simulation of resolved structures in an Eulerian two-fluid framework”, Nucl. Eng. Des., 305, 2016, pp. 371–377.

[17] J. Adelsberger, P. Esser, M. Griebel, S. Groß, M. Klitz, A. Rüttgers, “3D Incompressible Two-Phase Flow Benchmark Computations for Rising Droplets”, Proceedings of the 11th world congress on computational mechanics (WCCM XI), Barcelona, Spain, vol. 179, 2014, p. 1401.